25. Zero-g Processing of Magnets

Experiment MA-070

D. J. Larson, Jr.[a]

ABSTRACT

The Zero-g Processing of Magnets Experiment (MA-070) was conducted during the Apollo-Soyuz Test Project mission to study contained solidification of high-coercive-strength magnetic materials in the low-g orbital environment. The magnetic compounds under study, manganese bismuth (MnBi) and copper-cobalt-cerium ($(Cu, Co)_5$ Ce), are representative of magnetic alloy systems that have the potential for the development of high coercive strength and high energy product.

The samples of 50 atomic percent (at.%) Bi-50 at.% Mn solidified in the low-g environment demonstrated a substantial improvement in the macroscopic chemical homogeneity. The Bi/MnBi directionally solidified eutectic flight samples exhibited markedly superior magnetic properties. Intrinsic coercive strengths in excess of 14 722 kA/m (185 kOe) have been measured in the low-g processed samples at a temperature of 77 K. This strength exceeds the maximum previously published value (8992 kA/m (113 kOe)) by 64 percent. The average value of inductance was improved by 76 percent and the energy product by 57 percent.

Additional results of this experiment indicate that, in the near absence of the gravitational body force, contained fluids will assume a lowest energy configuration that differs significantly from that found terrestrially. These results are of significance to any orbital processing that involves controlled heat transfer to, or from, a contained fluid.

[a]Grumman Aerospace Corporation, Bethpage, New York; Principal Investigator.

INTRODUCTION

Although permanent magnets are essential to present-day technology, their importance is often overlooked. In fact, since the magnets are usually located inside equipment, most people either are not aware of their presence or take them for granted. However, these permanent magnets are the key components in many devices that are important to everyday life, such as telephone receivers, computers, radar equipment, loudspeakers, electrical meters, microphones, tape recorders, hearing aids, electric clocks, scientific instruments, magnetic door catches, and even children's toys (refs. 25-1 to 25-5).

In recent years, significant improvements in magnetic properties have resulted from the discovery of the exceptionally high anisotropy constants in compounds of cobalt (Co) and platinum (Pt) and of manganese (Mn) and bismuth (Bi) and in the cobalt-rare earth (RE) (and yttrium) systems (refs. 25-6 to 25-8). The magnitude of these improvements can be seen from table 25-I, in which the properties of some commercial magnets are compared with experimentally determined values of high-anisotropy magnets (ref. 25-9).

Because anisotropy energy results from the coupling between the spin of an electron and its orbital motion, the superior magnetic properties of high-anisotropy compounds are related to their crystal structures. The electron orbits are strongly directional and are associated with the lattice symmetry.

Most high-anisotropy compounds have a complex hexagonal lattice symmetry. The C-axis is the unique direction of easy magnetization, and the

TABLE 25-I.—Physical Properties of Magnetic Materials

Material	*Energy product* $(BH)_{max}$ *MTA/m (MGOe)*	*Coercive strength* H_c, *kA/m (kOe)*	*Curie Temperature, K (°C)*
Alnico	79 577 (10)	159.2 (2)	973 to 1073 (700 to 800)
Barium ferrite	31 931 (4)	238.7 (3)	996 (723)
CoPt	71 620 (9)	397.9 (5)	783 (510)
MnBi (directionally solidified)	[a]58 092 (7.3)	2387.3 (30)	623 (350)
Co_5-RE	[b]190 986 (24)	[bc]795.8 (10)	[b]1143 (870)

[a]Powders.

[b]Typical values. [c]Values as high as 2228.2 kA/m (28 kOe) were obtained in chill cast specimens of Co_3Cu_2Sm (ref. 25-10).

directions within the basal planes are uniformly hard to magnetize (ref. 25-9). The excess energy required to turn the direction of magnetization from an easy direction to a hard direction is the anisotropy energy. The anisotropy constant K is a measure of this energy and is related to the theoretical upper limit of the coercive strength

$$H_A = \frac{2K}{M_s}$$

where M_s is the saturation magnetization (ref. 25-11). Values of K range from 5 to 12 J/cm^3 (5 to 12 $\times$ 10^7 ergs/cm^3) for Co_5- RE-type compounds (refs. 25-4 and 25-9) and result in values of H_A from 11 937 to 19 894 kA/m (150 to 250 kOe). Besides the high anisotropy constants and high coercive strength, permanent magnets also must have a high intrinsic magnetization ($4\pi M_s$) and a high Curie temperature (T_c).

Because of the brittleness and reactivity of most magnetic compounds, powder metallurgy techniques principally have been used to fabricate high-coercive-strength magnets. Casting and solidification techniques have been possible only in a limited number of systems.

Fabrication of high-coercive-strength magnet materials from the liquid state could lead to a marked reduction in the number of processing steps and hence in cost. The magnets would have theoretical density, the fine particles would be protected from environmental attack, the magnets would have a high degree of particle alinement, and the magnets would only require a minimal amount of final machining. The requirement of particle refinement and crystallographic and magnetic alinement has led several investigators to consider directional solidification as a means of achieving this morphology.

In space, gravity-driven convection and gravitationally dependent elemental segregation are absent in the liquid state. This fact has important consequences in the directional solidification of eutectic alloys. When grown on Earth, the rod or lamellar structure of the eutectic usually contains many imperfections (faults or terminations) due to local thermal and compositional gradients resulting from convection. It has been suggested that eutectic solidification in the absence of gravity will produce better alinement and fewer imperfections as a result of the reduction of these convection currents. Directional solidification in the orbital environment would then improve the magnetic coercivity and, perhaps, the energy product. The work reported here was undertaken to test the effect of the reduction of gravitationally dependent elemental segregation and convection on high-coercive-strength magnetic composites.

EXPERIMENTAL PROCEDURE

Three sets of three samples were simultaneously processed in the course of this experiment. Three furnace cartridges, each housing three samples, were used. The sample arrangement within the furnace and each cartridge is shown in figures 25-1 and 25-2. Ampoules 1 and 2 were made from pyrolytic boron nitride; ampoule 3 was composed of fused silica (quartz). The thermal processing

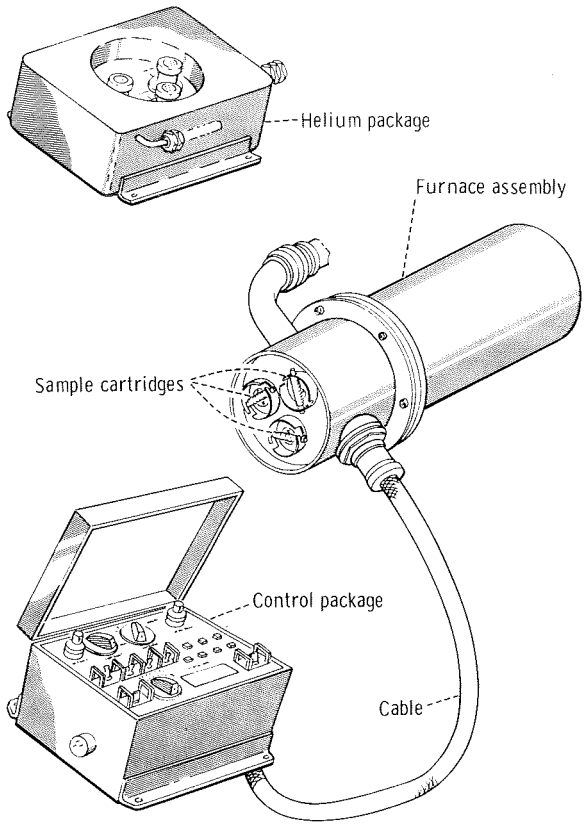

FIGURE 25-1.—The ASTP multipurpose electric furnace system.

was conducted in the multipurpose furnace (ref. 25-12) located in the Apollo-Soyuz Test Project (ASTP) docking module.

Experiment planning was based on thermal results from the prototype test. It was anticipated that the thermal environment for ampoule 1 (fig. 25-2) would be essentially isothermal over the temperature range of solidification. Ampoule 2 was expected to be exposed to a thermal gradient of 30 ± 2 K/cm and ampoule 3 to a thermal gradient of 60 ± 3 K/cm. The flight samples were actually exposed to conditions substantially different from planned conditions, and these differences will be detailed in the following paragraphs.

The prototype test was the only thermal test of the furnace cartridge that was internally instrumented with thermocouples. The prototype furnace differed from the flight furnace in that it was a single-tube furnace. The flight furnace was a three-tube furnace with the tubes equidistant from the centerline of the furnace and arrayed 120° apart. The geometrical difference between the prototype, ground-based, and flight furnaces resulted in the last two experiments being conducted in thermal environments that were not radially symmetric. This characteristic will be considered further in the section entitled "Phase Relations and Microstructure."

The longitudinal thermal profiles from the prototype test are shown in figure 25-3; T_{HL} is the heat-leveler temperature. The furnace temperature histories for the ground-based and flight tests are shown in figure 25-4. The time to reach operating temperature for the flight test was longer than that for the ground-based test, and the hold time was slightly shorter (45 minutes compared to 60 minutes). The cooling rate was greater during the flight test. Because all samples are completely solidified at helium injection, the differences in cooling rate after helium injection are not very significant.

The thermal history deduced for the type 1 flight ampoules is shown in figure 25-5. Because thermal data of this type were not provided for the ground-based test, no direct comparison can be made. It is safe to conclude, however, that the cooling rate of the flight samples was, on the average, 10 percent greater than that of the ground-based samples. The difference in cooling rate was greatest for ampoule 1 and least for ampoule 3.

The thermal gradient was calculated, as a function of time, for ampoule 2 and 3. These calculations were made from analytical data presented in reference 25-13. The variation of the thermal gradient, including the time during which the samples in the type 2 ampoules were directionally solidifying, is shown in figure 25-6. The temperature gradient for ampoule 2 varies from approximately 30 K/cm at the onset of directional solidification to 23.5 K/cm at the conclusion of solidification.

The variation of the thermal gradient in ampoule 3 (ref. 25-13) is shown in figure 25-7 for the lifetime of the experiment, and in figure 25-8 for the duration of the directional solidification. The thermal gradient during the period of maximum superheating was 80 K/cm; however, during the period of solidification, it varied from only 10.9 K/cm at the onset to 8.9 K/cm at the conclusion.

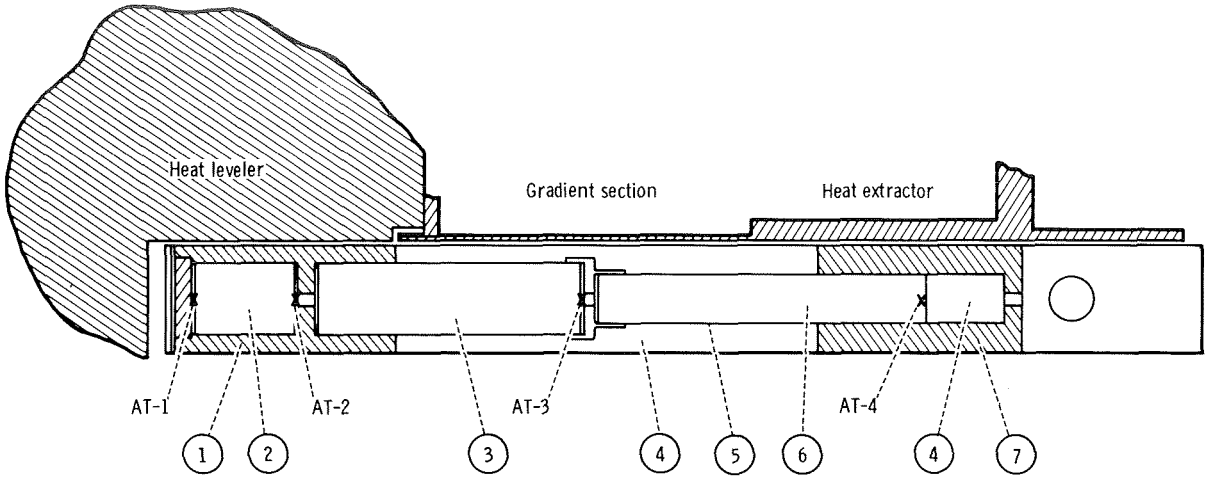

1. Thermal insert, ZTA graphite
2. Ampoule 1
3. Ampoule 2
4. Insulation
5. Support tube, 321 stainless steel
6. Ampoule 3
7. Thermal insert, ZTA graphite

FIGURE 25-2.—Experiment MA-070 cartridge.

The value during solidification is lower than the thermal gradient anticipated from the prototype test by approximately 80 percent.

EXPERIMENTAL RESULTS

Fluid Statics

The fluid state before and during thermally controlled solidification is of critical importance to successful plane-front solidification of single-phase and polyphase alloys. This fluid state is complex and involves both static and dynamic components. Many of these fluid effects can be shown to be functionally dependent on gravity vector and level; therefore, it would be anticipated that orbital processing would have a substantial influence on them. The measurements required to conduct *in situ* and postflight dynamic analyses of the flight samples, processed during the ASTP flight, were deemed impossible. Thus, only static fluid analysis was conducted.

Previous orbital plane-front solidification experiments, performed during the Skylab Program,

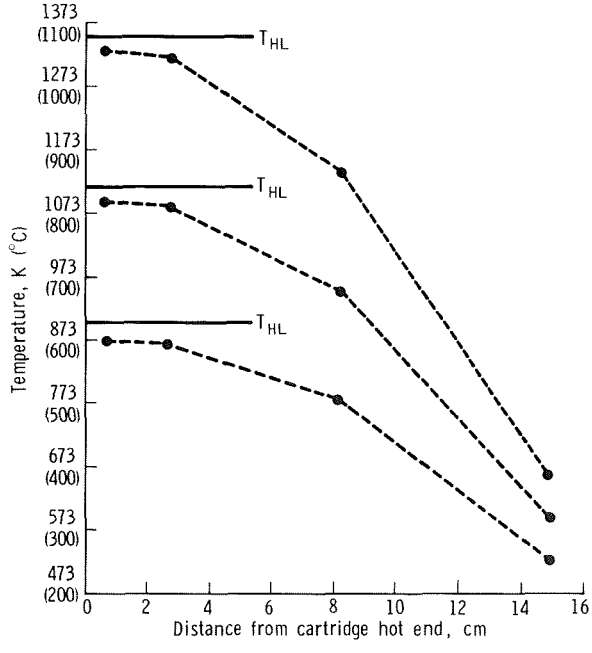

FIGURE 25-3.—Longitudinal temperature distribution within experiment cartridges; prototype test results.

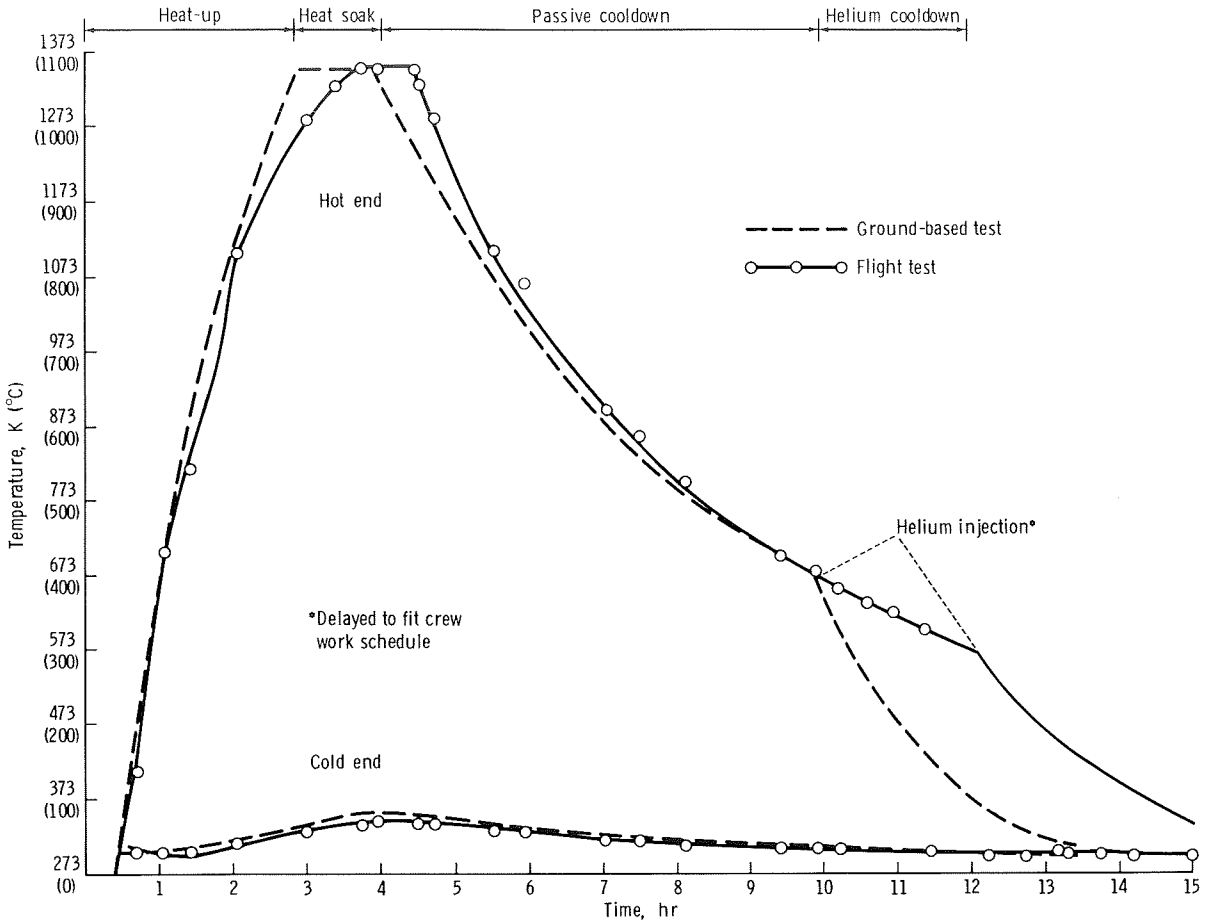

FIGURE 25-4.—Furnace temperature compared to elapsed time for the ASTP ground-based and flight tests.

indicated that the static fluid shape in the orbital environment was appreciably different from the static fluid shape documented terrestrially (refs. 25-14 and 25-15). If the static fluid configuration is changed, the heat flux, the thermal profile, and the solid/liquid-interface geometry may also change. Because these factors are critical to the plane-front solidification process, the success or failure of the experiment may depend on anticipating these changes. Previous work conducted in the drop tower facility at NASA Lewis Research Center (LeRC) has identified the fluid-crucible variables that are of primary consideration in a reduced gravity environment (refs. 25-16 to 25-18). The variables cited in the LeRC work are the fluid/crucible wetting angle θ, the thermal gradient G, the crucible taper, the fluid/crucible fill factor, the crucible diameter to length ratio D/L, the gravity vector $\mathbf{g}$, and the magnitude of the gravitational acceleration $|g|$ (refs. 25-4 to 25-6). The LeRC results on fluid displacement are presented schematically in figure 25-9, and the static fluid configurations and displacements within a cylindrical crucible are illustrated in figure 25-10.

The fluid statics analysis of the samples was initiated while the flight ampoules were still in place in the experiment cartridges. Before the cartridges were disassembled, each was radiographed twice, at 90° angles, and the results were interpreted. A representative radiograph of the three cartridges is shown in figure 25-11. Several points to be noted in figure 25-11 will be detailed in subsequent sections, but may be summarized as follows.

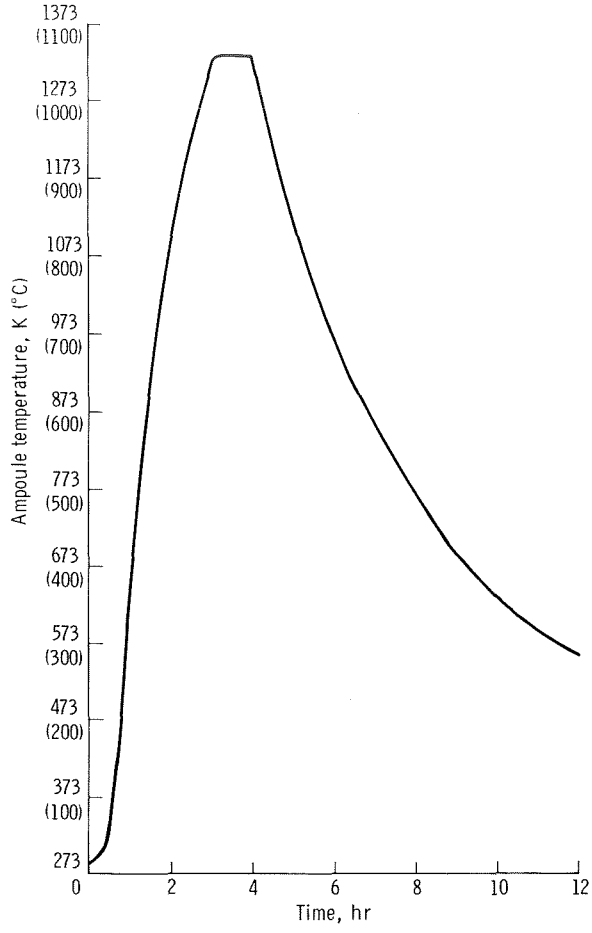

FIGURE 25-5.—Temperature profile for type 1 flight ampoules.

1. The type 1 samples (fig. 25-2) are of differing configurations, and the sample in cartridge 9 has leaked from the inner to the outer crucible.

2. The type 2 samples appear similar, but the sample in cartridge 8 appears higher than the other two.

3. The type 3 samples appear to be at differing heights. The sample in cartridge 9 is the highest, and that in cartridge 8 is the lowest. It is apparent that some material has been lost from ampoule 3 in cartridge 9, and subsequent analysis showed that some material had been lost from ampoule 3 of cartridge 7 as well. These displacement and configurational differences are all explicable on the basis of figures 25-9 and 25-10.

The fluid in the type 1 ampoules (50 atomic percent (at.%) Bi, 50 at.% Mn) wet the inner crucible (pyrolytic boron nitride), and the crucible had a diameter-to-length ratio of approximately 0.71. The volumetric fill factors were varied within the type 1 ampoules, and the samples were processed isothermally ($G = 0$). The fill factor for the ampoule within cartridge 7 was 0.95, that within cartridge 8 was 0.90, and that within cartridge 9 was 0.85. It was anticipated that variation from type 1 to type 4 fluid configuration would be noted (fig. 25-10). Unfortunately, the sample in cartridge 9 was lost through a vibrational failure; however, samples 7 and 8 were consistent with type 1 and intermediate configurations (type 1/type 4 behavior). This result was indicative of a low wetting angle, as previously mentioned.

The type 2 ampoules housed a wetting liquid (8 at.% cerium (Ce), 92 at.% copper (Cu) and cobalt (Co)) within a crucible. These samples, which were processed in a thermal gradient of approximately 27 ± 2 K/cm, were not totally melted, but were melted back along the seed crystal such that, at peak furnace temperature, the fluid was in contact with a seed crystal. Figure 25-9 shows that a wetting fluid would be expected to be displaced toward the colder end of a thermal

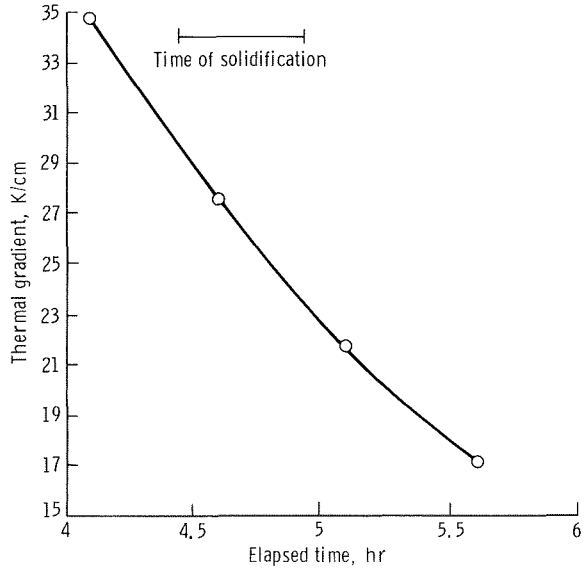

FIGURE 25-6.—Thermal gradient as a function of elapsed time for type 2 flight ampoules.

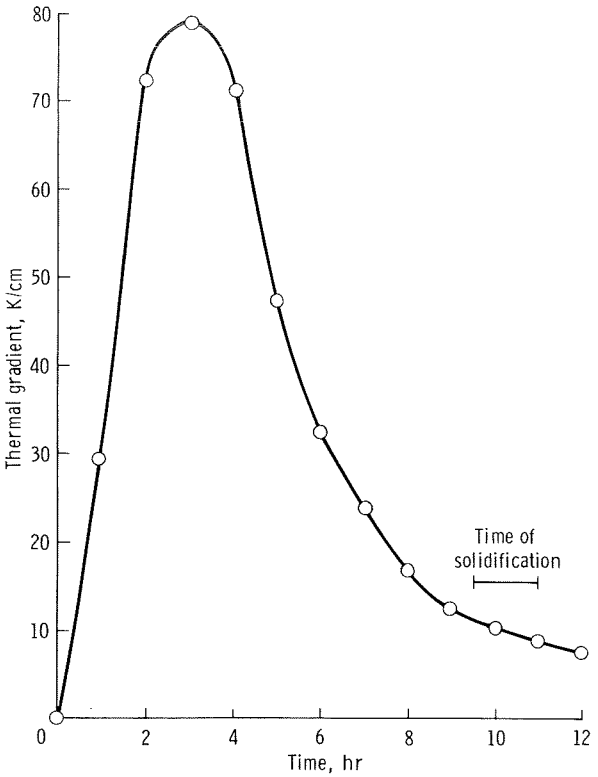

FIGURE 25-7.—Thermal gradient as a function of time for type 3 flight ampoules.

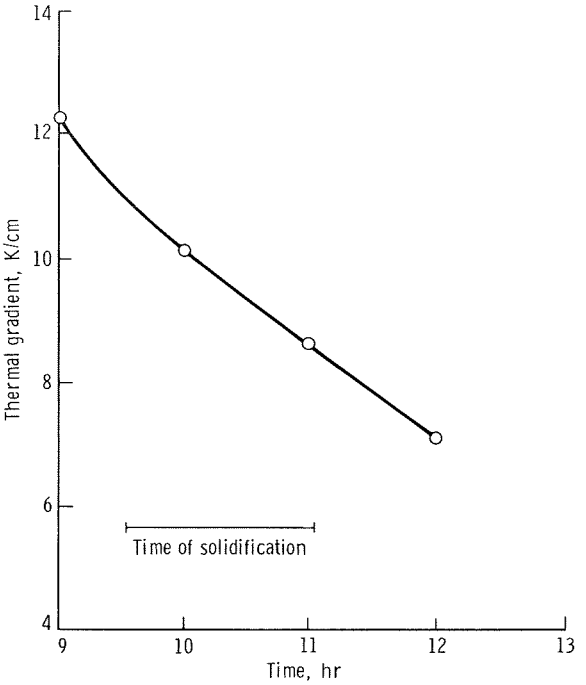

FIGURE 25-8.—Thermal gradient during time of solidification of type 3 flight ampoules.

gradient; that is, toward the seed crystal. Because the seed crystal would be mechanically fixed, no fluid displacement would be expected. Therefore, the upward displacement of sample 2 in cartridge 8 must be explained on the basis of mechanical displacement of the entire seed crystal, prior to the melting and solidification sequence.

The type 3 ampoules were intended to demonstrate the behavior of an unconstrained (no seed crystal), nonwetting fluid (97.8 at.% Bi, 2.2 at.% Mn) in a thermal gradient. The thermal gradient varied from 80 to 10 K/cm during the experiment. These fused silica ampoules had been backfilled

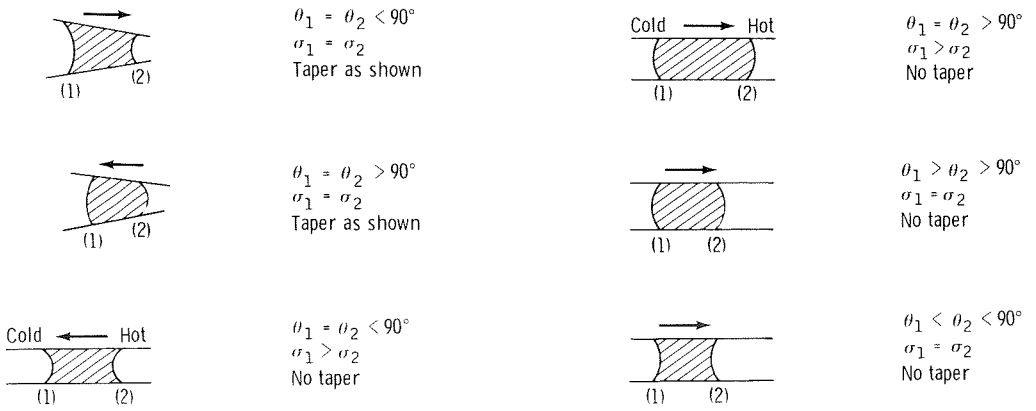

FIGURE 25-9.—Results on fluid displacement in a reduced gravity environment, where σ is surface tension.

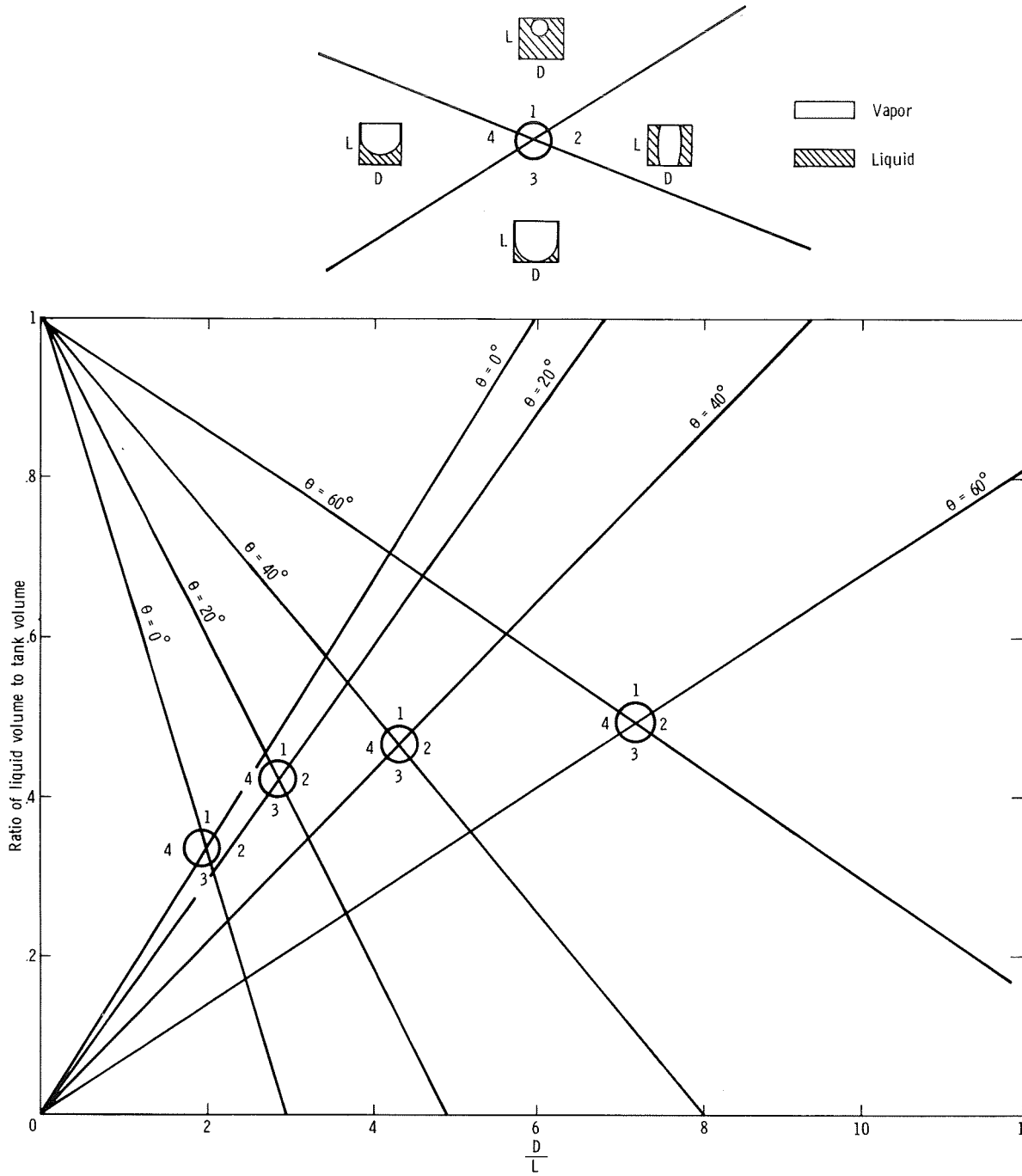

FIGURE 25-10.—Wetting fluid configurations in a cylindrical tank.

with an inert gas (argon) to suppress the possibility of thermal cavitation of the bismuth-rich liquid. Apparently, in the backfilling operation, a small amount of contaminant oxygen was allowed to enter ampoule 3 of cartridge 8. This small amount of oxygen was sufficient to alter the

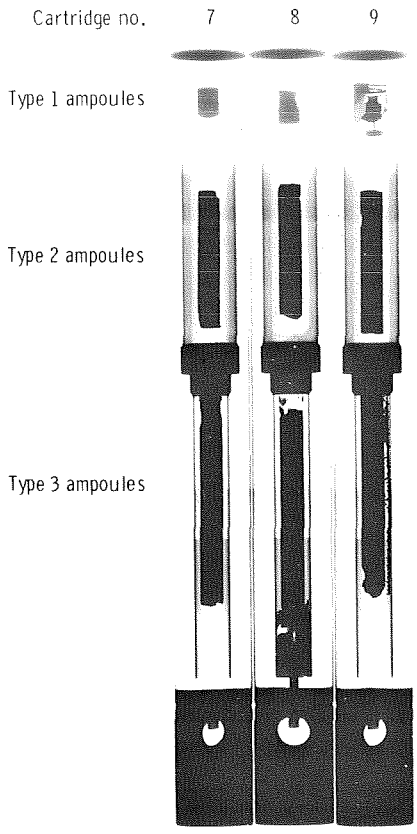

FIGURE 25-11.—X-ray radiograph of the three flight cartridges.

characteristics of the fluid/crucible interface from nonwetting to wetting, with concomitant changes in the fluid displacement behavior.

As would be anticipated from figure 25-9, the nonwetting fluid moved toward the hot end of the ampoule, whereas the wetting fluid moved in the opposite direction. This relative fluid displacement has been mentioned previously. Fluid displacement in the outermost ampoules resulted in the failure of the ampoules. The bismuth-rich fluid expands on solidification. The movement of the fluid toward the hot end of the ampoule resulted in a condition, during the latter stages of solidification, characterized by insufficient free volume in the ampoule to house the resultant solid. The pressure buildup within the ampoules was sufficient to cause cracking. This result should be considered in the planning of subsequent solidification experiments in which the fluid expands on solidification.

Phase Relations and Microstructure

The thermal profile imposed on the type 3 ampoules substantially superheated the bismuth-rich liquid when the furnace was at peak temperature. This superheating necessitated the previously mentioned backfilling operation. To check the compatibility of the quartz ampoule with the superheated bismuth-rich liquid, quartz-bismuth samples were superheated within a differential thermal analysis unit. Results of these studies confirmed the compatibility of the bismuth and quartz at temperatures as high as 1050 K and determined that a liquid phase transition occurred in the liquid bismuth. Similar fluid-state transitions have been reported for other semimetals (ref. 25-19), but not previously for bismuth. The bismuth transition was characterized by large temperature hysteresis and was rate sensitive. At a rate of 10 K/min, the transition occurred at 988 K (715° C) on heating and 858 K (585° C) on cooling.

The samples within the type 1 ampoules (fig. 25-2) were composed of 50 at.% Bi and 50 at.% Mn. Three Bi-Mn phase diagrams have been proposed (refs. 25-20 to 25-22); all three were considered in this experiment. Ground-based investigation before the ASTP flight supported the liquidus results of references 25-21 and 25-22. Investigation performed in the analysis of the flight samples indicates that the phase diagram of reference 25-22, shown in figure 25-12, is preferable. This conclusion is based on qualitative metallographic evidence, and quantitative thermal and chemical analysis is in progress. The quantitative data will determine whether this preliminary conclusion is sound.

The samples in the type 1 ampoules, henceforth denoted as type 1 samples, were processed by isothermal lowering ($G = 0$) from a temperature above the liquidus temperature. A characteristic of the ground-based samples was appreciable gravitationally dependent macrosegregation. This chemical macrosegregation resulted in the location of almost all the primary properitectic

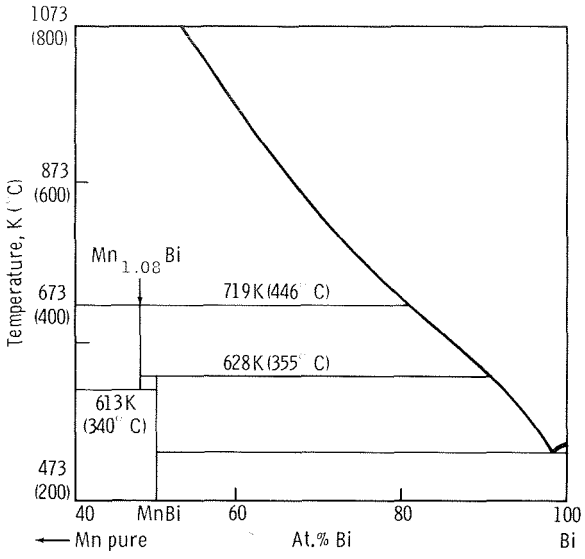

FIGURE 25-12.—Proposed Bi-Mn phase diagram (ref. 25-22).

Mn particles at the top of the sample. The volume fraction of the MnBi phase, determined by quantitative areal analysis, continuously decreased from the top of the ingot to the bottom. This variation, for a ground-based sample exposed to the same thermal cycle as the flight samples, is shown in figure 25-13. The average value for this sample was 29.5 volume percent of primary Mn and MnBi particles. The volume fraction of the primary MnBi phase in the flight samples was more uniformly distributed, and no primary Mn particles were identified. The average volume fraction of primary particles (fig. 25-13) was 35.7 percent, which may be an indication that the peritectic Mn had reacted with the Bi-rich liquid to form MnBi. Because the samples are being conserved for detailed magnetic analysis (discussed in the following subsection), these measurements were made only on the upper and lower ends of the samples.

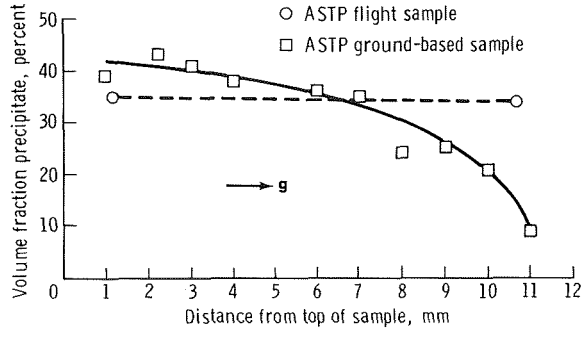

FIGURE 25-13.—Precipitate volume fraction as a function of distance from top of ground-based and flight samples.

The flight samples were found to have large primary MnBi particles, lying on or near the surface, transverse to the longitudinal direction of the samples. This characteristic was unexpected and was not typical of the ground-based samples. The structure might indicate that the radial gradient experienced by the flight samples was greater than the longitudinal gradient and thus caused the primary crystallites to grow radially, in the direction of heat extraction. It is possible that gravitationally dependent convective flow caused a more uniform thermal distribution in the ground-based samples, or at least prevented alinement of the primary crystallites.

Some of the ground-based and low-g primary MnBi crystallites appeared to be composed of two distinctly different microstructural regions, as shown in figure 25-14, whereas others did not. This anomaly can be explained on the basis of the phase diagram shown in figure 25-12, in which two compositional modifications of MnBi are proposed. The first, MnBi (I), forms at a temperature of 719 K (446° C) and is manganese rich. The stoichiometric ratio proposed for this compound is $Mn_{1.08}Bi/Bi_{1.00}$. This phase decomposes eutectoidally to MnBi (II) plus Mn at a temperature of 613 K (340° C). The MnBi (I) phase forms directly from the melt at a temperature between 719 K (446° C) and 628 K (355° C). The MnBi (II) phase is equiatomic and forms directly from the melt at a temperature between 628 K (355° C) and 542 K (269° C), the eutectic temperature.

When the flight samples are considered, the crystallites forming at temperatures between 719 K (446° C) and 628 K (355° C) would be expected to react with residual liquid between 628 and 613 K to form MnBi (II). This reaction would be subject to the same diffusion barrier limitations common to all peritectic or peritectoid reactions and would not be expected to go to completion. The MnBi (I) core would then thermally decompose at a temperature below 613 K (340° C) to Mn plus MnBi (II). The MnBi (II) formed by way of the

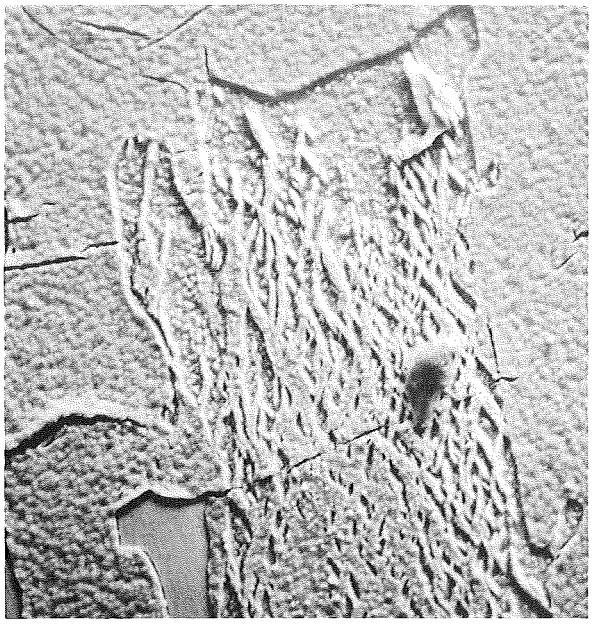

FIGURE 25-14.—Primary MnBi crystallite showing discrete morphological regions (900×).

peritectic reaction would then act as a heterogeneous nucleus for continued MnBi (II) precipitation at a temperature below 628 K (355° C). Sections of crystallites undergoing the preceding sequence would be expected to have a duplex appearance. The MnBi (II) formed at a temperature below 628 K (355° C), by way of either peritectic reaction (fig. 25-15(a)) or proeutectic precipitation (fig. 25-15(b)), would be expected to appear monolithic, whereas residual MnBi (II) would be expected to show some evidence of the eutectoid decomposition. Crystallites forming at a temperature below 628 K (355° C) would be expected to be monolithic throughout.

The secondary MnBi (II) crystallites were found to be almost normal to the primary MnBi crystallites in the low-g samples (fig. 25-15(a)), whereas they were typically skewed in the one-g samples (fig. 25-15(b)). This may be an indication of decreased fluid motion, although other hypotheses may be proposed to explain the phenomenon.

In addition to having morphological differences, the secondary crystallites were finer in the flight samples than in the ground-based samples. One might have expected the opposite to be true because the rate of cooling through this temperature range was slower for the flight samples than for the ground-based samples. (See figure 25-4).

Processing of the samples in the type 2 ampoules was hampered by experimental limitations. The peak furnace temperature available was 1323

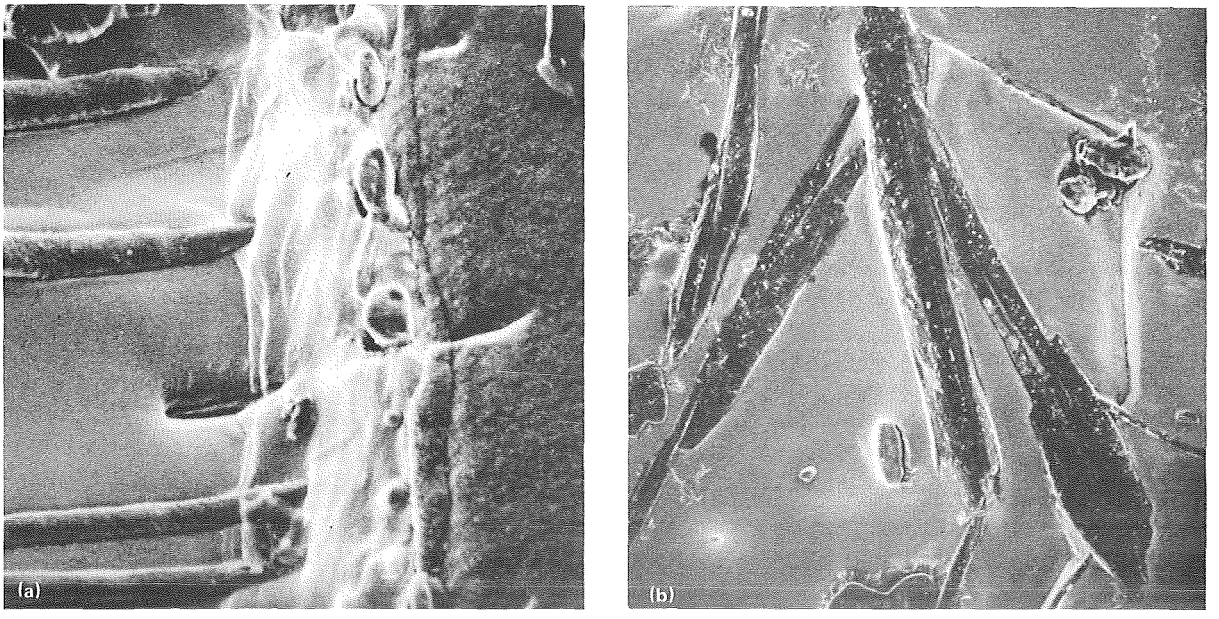

FIGURE 25-15.—Primary and secondary MnBi particles. (a) Flight sample (3750×). (b) Ground-based sample (1500×).

K (1050° C). To process most metallic-rare earth ($M_5 - RE$) compounds would have required a furnace temperature of 1773 K (1500° C) to 1873 K (1600° C). This experimental constraint required that a serious alloy development program be undertaken. In the development program, varying combinations of copper, cobalt, and iron were considered as the metallic component, and varying combinations of cerium, samarium, and misch metal were considered as the rare earth component. On the basis of the alloy development data,[1] the maximum copper content, with cerium or misch metal alloying additions, provided the lowest liquidus temperatures, but sacrificed magnetic performance to experimental expediency.

In addition to thermal problems, crucible/fluid compatibility problems were encountered. In short, all rare earth liquids are extremely reactive and hence difficult to contain. The results of ground-based studies and literature surveys identified pyrolytic boron nitride as the most promising crucible material. This crucible material did react with the melt but seemed to establish a stable reaction product at the crucible/fluid interface that acted as a barrier to further reaction. Results of ground-based studies showed that the copper-cerium fluid was the least reactive of the fluids investigated.

The thermal and compatibility considerations, in concert, dictated selection of the copper/copper-cerium eutectic as the eutectic composite material for this experiment.

Analysis of the samples processed in the type 2 flight ampoules indicated that directional solidification was not achieved in this experiment. The reaction product at the fluid/crucible interface acted as a heterogeneous nucleation point ahead of the advancing solid/liquid interface, and coordinated eutectic growth was not achieved. Crystallites grew into the melt from the crucible wall.

Directional solidification of high-performance rare earth magnetic composites in orbit is still considered by the author to be an attractive possibility. Ideally, however, it would be conducted in a floating-zone directional-solidification apparatus that could impose steep thermal gradients on the samples and achieve an absolute temperature of 2000 K (≈1750° C). This would eliminate most of the experimental constraints, and the experiment could be performed properly.

The samples in the type 3 ampoules, henceforth denoted type 3 samples, were 97.8 at.% Bi and 2.2 at.% Mn, the eutectic composition. These samples were totally melted and were solidified in a temperature gradient of approximately 10 K/cm. Although the temperature gradient was substantially lower than anticipated, coordinated eutectic growth was achieved.

The microstructure in the region of initiation of solidification of ground-based and flight samples consisted of large primary bismuth dendrites with Bi/MnBi (II) eutectic in the interdendritic regions. The eutectic in this region was not well alined with the imposed thermal gradient, as is shown in figure 25-16 for a ground-based sample. As the solidification progressed in the ground-based and flight samples, the primary bismuth dendrites became fewer in number and the interdendritic eutectic became progressively better alined with the thermal gradient, as shown in figure 25-17 for

FIGURE 25-16.—Primary bismuth dendrites and secondary MnBi/Bi eutectic (650×).

[1] D. J. Larson, Jr., ASTP MA-070 Experiment Final Report, in press.

FIGURE 25-17.—Primary bismuth dendrites and alined secondary MnBi/Bi eutectic (325×).

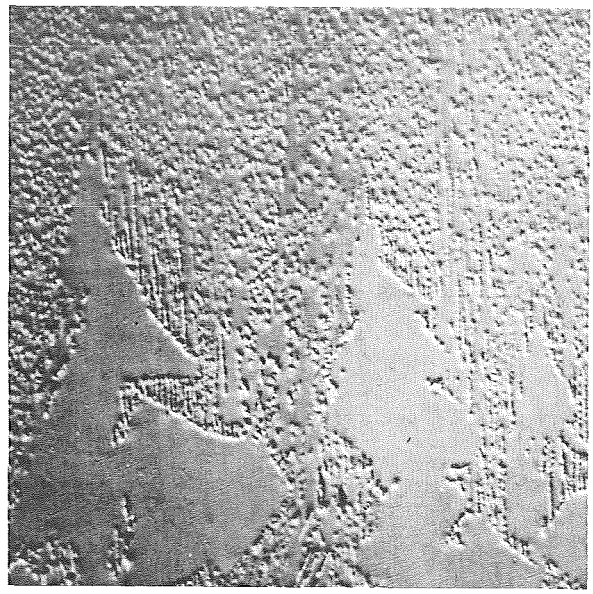

FIGURE 25-18.—Transition from dendritic to coordinated growth (75×).

a ground-based sample. Ultimately, there was a transition from dendritic to coordinated growth in both sample sets, as shown in figure 25-18 for a ground-based sample. The latter region of uniformly distributed and alined magnetic particles was analyzed magnetically.

The Bi/MnBi eutectic system is a doubly faceted system (ref. 25-23). The rod shape, in cross section, is dependent on the growth rate during solidification. At slow growth rates, the rods have a cross section reminiscent of a chevron; whereas, at rapid rates, the cross section is nearly circular.

The rod cross section of the ASTP ground-based samples was chevronlike, as shown in figure 25-19. This result is consistent with previous findings (ref. 25-24). The rod diameter, however, was smaller in the flight samples than in the ground-based samples, and the cross section was circular. Particle sizes in the flight samples were typically 0.75 to 2.00 μm, whereas the ground-based samples had particles of 2.0 to 4.0 μm diameter. This result is somewhat surprising as it is generally understood that the rod diameter varies in a manner such that the square of the diameter (d^2) times the growth rate R is a constant, over wide ranges of

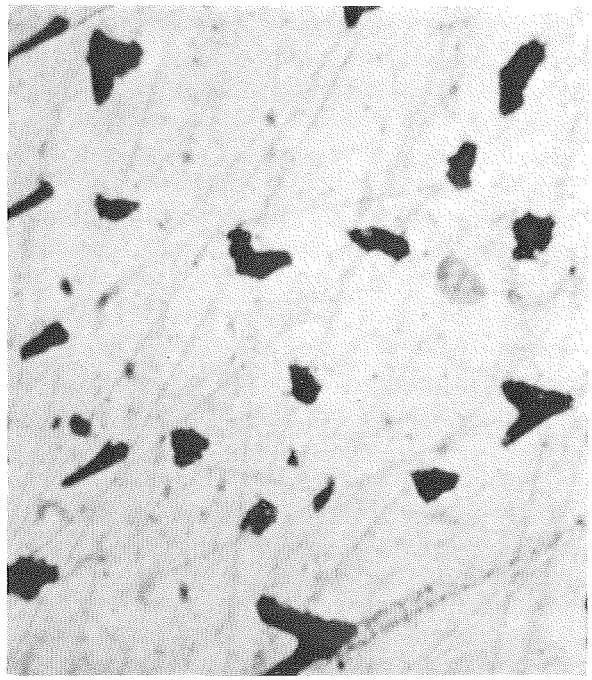

FIGURE 25-19.—Transverse section of ASTP flight sample 8C (2000×).

growth conditions (ref. 25-25). It was not anticipated that the growth rate would vary significantly between the ground-based and flight experiments; therefore, the cause for this variation in d would seem to reside within the "constant," which was not expected to vary.

Consideration of the various possibilities that would lead to a difference of this magnitude is continuing. One distinct possibility is thermal transport, which should be enhanced in a convectionless environment. This could impact both the solute profile ahead of the advancing interface (i.e., the diffusional coefficient in the previously mentioned constant) and the dendritic to coordinated transition. Although thermal transport would seem to be a likely source of difference, the lower limit of influence has been predicted analytically (ref. 25-26) and the experimental parameters for the ASTP flight experiment would seem to predict only a small influence. Investigation in this area will be pursued.

The refinement of the particle size in the flight experiment was also reflected in the magnetic results. These results will be detailed in the following subsection; however, it is important to note that the flight samples behaved magnetically like samples grown terrestrially about six times faster. This is equivalent to saying that, if d^2 was determined by the ratio of the constant to the growth rate, then, for magnetic equivalence, the flight samples should have a particle diameter approximately 40 percent of the ground-based value. This conclusion is reasonably consistent with the particle size data, when the scatter bands are considered.

Another set of measurements was made to compare the flight samples with the ground-based samples. These measurements were of the MnBi lattice parameter. It was assumed in these measurements that all the MnBi used had 4 atoms/unit cell and was of a $D^4_{6h} - P6_3/mmc$ hexagonal structure. The bismuth was assumed to have 2 atoms/unit cell and a $D^5_{3d} - R\bar{3}m$ structure. A bismuth rhombohedral angle α of 57°14′ was assumed throughout this study.

Measurements based on the MnBi {10 · 0} and {21 · 0} reflecting planes were used to calculate the MnBi lattice parameters. Because of the low volume fraction and crystallographic anisotropy of the samples, it was impossible to consistently use lines other than these. The lattice parameter measured from the ground-based samples, in the coordinated growth region, was $a_0 = 0.4255 \pm 0.0003$ nm (4.255 ± 0.003 Å). This value did not vary, within experimental error, over the length of the coordinated growth region. The value measured for the coordinated growth region of one of the flight samples was 0.4306 ± 0.0003 nm (4.306 ± 0.003 Å). This difference is well beyond experimental error and is worthy of further consideration.

Slowly cooled bulk MnBi samples have been reported to have a_0 lattice parameters varying from 0.425 to 0.427 nm (4.25 to 4.27 Å). Rapidly cooled bulk samples, and samples quenched from high temperatures, have a_0 parameters as large as 0.433 nm (4.33 Å) (quenched from 673 K). The lattice parameter from the flight sample would indicate that it is equivalent to a sample quenched from an intermediate temperature or grown at a higher growth rate. This result is consistent with the investigator's magnetic and particle size conclusions.

Magnetic Analysis

The optimum morphological array for a magnetic composite consists of fine, elongated, single-domain magnetic particles alined in a matrix, with the easy axis of magnetization parallel to the particle axis (ref. 25-27). The greater the magnetocrystalline anisotropy constant for the magnetic phase, and the finer the discrete magnetic particles (ref. 25-28), the higher the magnetic coercivity.

Directional solidification of magnetic composites is promising because the particle size of the magnetic phase in a rod eutectic is typically on the order of 1 μm, the finely dispersed magnetic phase is protected from contaminating environmental effects, and the easy axis of magnetization of the magnetically anisotropic dispersed phase is frequently the crystallographic growth direction of the magnetic phase. Directional solidification of magnetic composites thus offers the potential for protection, alinement, and refinement of the dispersed magnetic phase.

As mentioned in the section entitled "Phase Relations and Microstructure," directional solidification was not achieved in the type 2 samples, and the magnetic properties of the ground-based and flight samples were essentially the same. The measured intrinsic coercivity H_{ci} of the magnetic phase was 82.8 kA/m (1.04 kOe) in both cases (within experimental error). As mentioned previously, the evolution of new experimental hardware is required to successfully accomplish the original goal of processing high performance rare earth magnetic composites.

The type 3 samples, however, were successfully processed; and because of their high performance, particularly at cryogenic temperatures, all measurements were made at the Francis Bitter National Magnet Laboratory of the Massachusetts Institute of Technology.

A typical Bitter magnet facility is shown in figure 25-20. The large cooling capability is required because 5 to 10 MW of power is passed through these magnets, depending on which unit is being used.

A standard two-coil pickup was used to make the measurements on the full length of the coordinated growth region. Sample sizes were approximately 2.5 cm long and 5 mm in diameter. A flux integration technique was used to map the B-H curves. The coil circuit used is shown schematically in figure 25-21 and the integrator circuit is shown schematically in figure 25-22. The H-axis was calibrated from the known calibrated field parameters, and B was calibrated using a VP grade pure nickel standard. Measurements were made with this diagnostic system at 295, 197, and 77 K. Thermal loss problems prevented the investigators from making lower temperature measurements with this apparatus. Measurements were made of field strengths as great as 18.5 T (185 kG).

A typical set of B-H loops for rapidly grown ground-based material, based on test temperature, is shown in figure 25-23. These curves are typical of directionally solidified MnBi dispersed in a Bi matrix. The duplex curve at 77 K was analyzed using the theory of superposition, and the data are

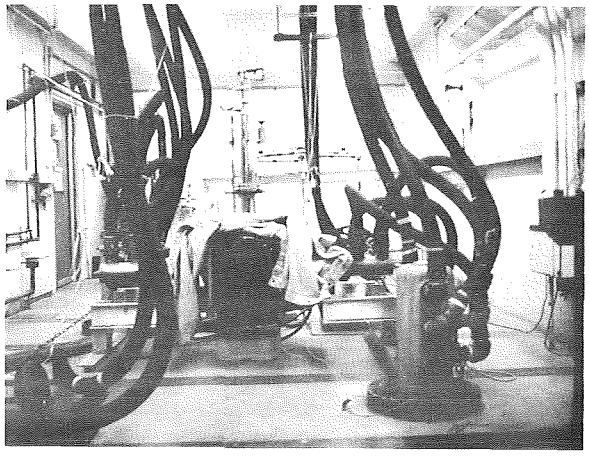

FIGURE 25-20.—Typical magnet facility at the Francis Bitter National Magnet Laboratory.

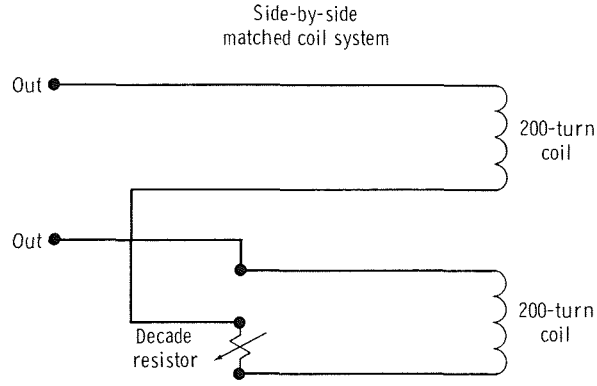

FIGURE 25-21.—Schematic of pickup coil circuit.

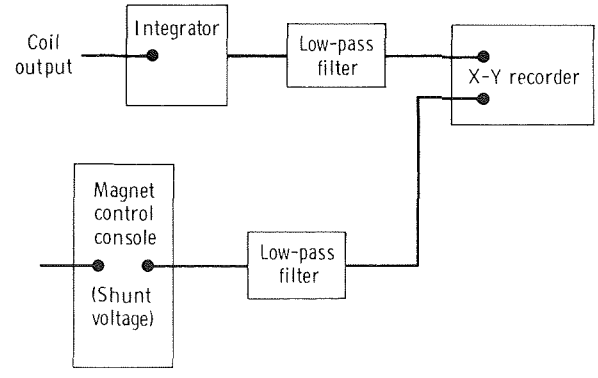

FIGURE 25-22.—Schematic of integrator circuit.

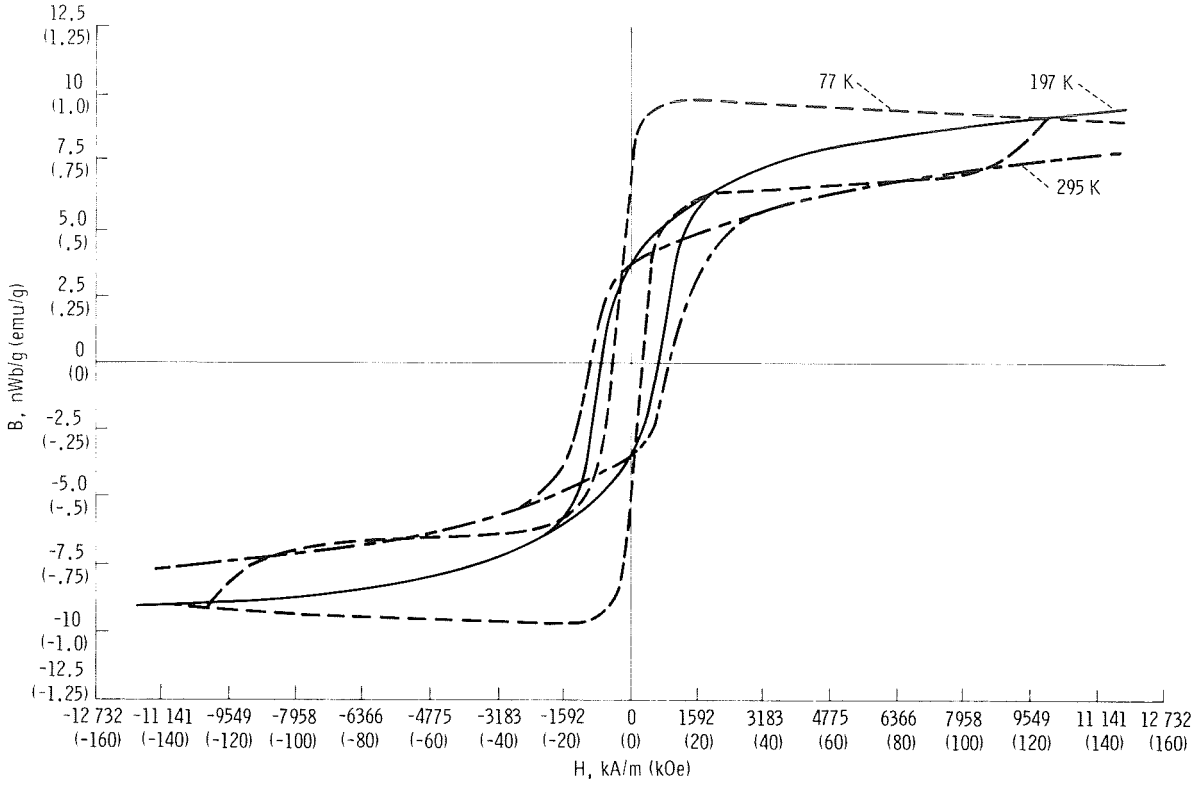

FIGURE 25-23.—Ground-based-sample MnBi/Bi eutectic composite B-H plot for three test temperatures.

reported in the manner of reference 25-24. The duplex loop reduces to two simple B-H loops as shown in figure 25-24.

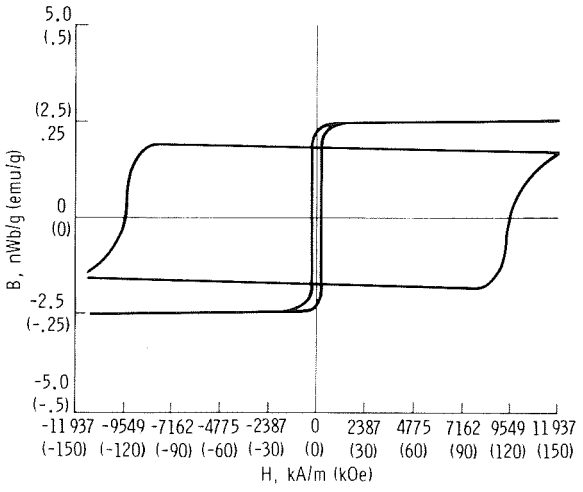

FIGURE 25-24.—Ground-based-sample B-H component loops at 77-K test temperature.

The apparatus previously described was relatively insensitive and prevented further reduction in sample size to enable more selective analyses in the coordinated growth region. A low-frequency vibrating-sample magnetometer was made available, and the general facility and the gearbox that changed the rotary motion to a vertical displacement in the field are shown in figures 25-25(a) and 25-25(b), respectively. The measurement technique and the hardware are fully described in reference 25-29. This apparatus substantially increased the resolution and enabled reduction of sample sizes by a factor of five. Also, measurements transverse to the magnetic flux lines could be made and the region of coordinated growth could be selectively analyzed. An additional advantage was use of the world's largest continuous-field magnet (23.5 T (235 kG)) and inclusion of measurements at a test temperature of 4.2 K.

The average room-temperature data for ground-based, flight, and literature samples are

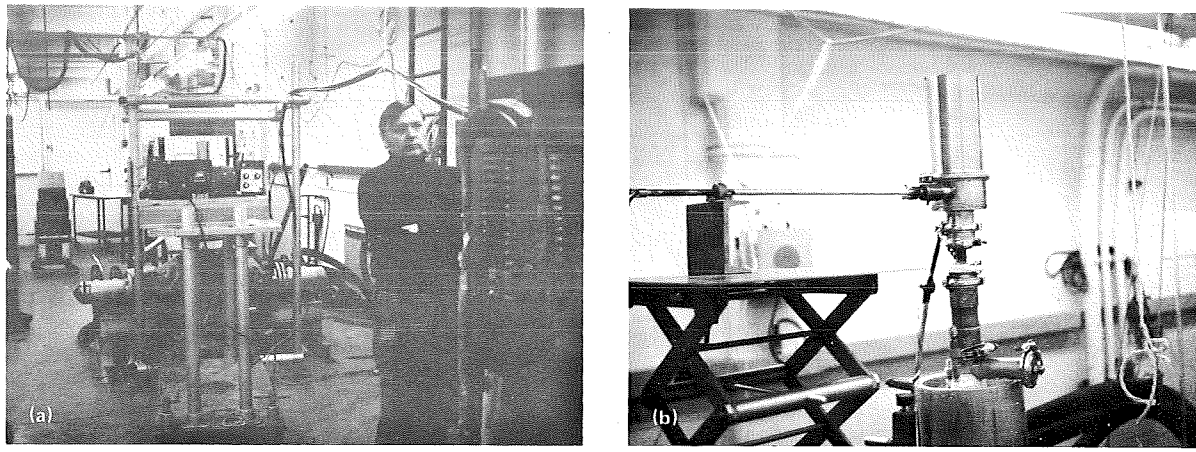

FIGURE 25-25.—Low-frequency vibrating-sample magnetometer. (a) Installation. (b) Gear mechanism.

presented in figure 25-26; the literature data are from reference 25-24. The square root of the growth rate was selected as the abscissa because it is a solidification parameter that should be proportional to the intrinsic coercive strength H_{ci}. It should be noted, however, that the literature data shown were measured on samples grown in a thermal gradient G an order of magnitude greater than that of this experiment. Although a steeper thermal gradient might be expected to impact the physical properties, no definitive study to quantify this effect has been made. To that extent, the comparisons are imprecise.

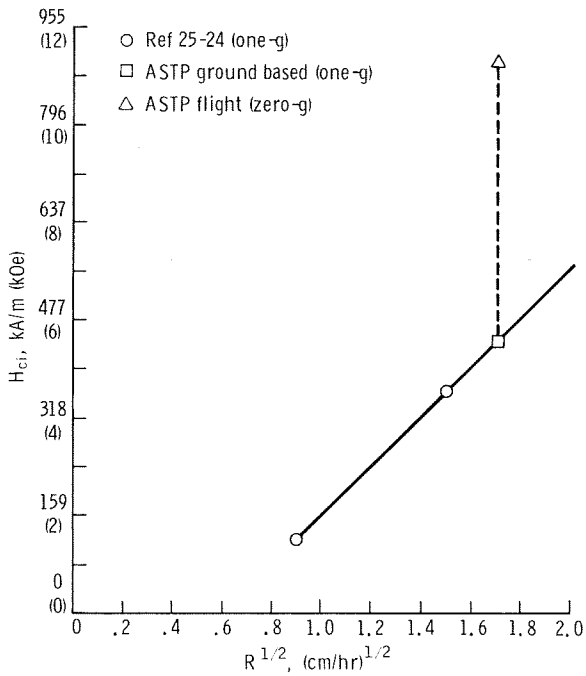

FIGURE 25-26.—Intrinsic coercive strength H_{ci} compared to the square root of growth rate $R^{1/2}$ for as-grown Bi/MnBi eutectic composites.

Representative B-H loops for ground-based samples have been shown for the eutectic composite at temperatures of 295, 197, and 77 K in figure 25-23. The configuration at 4.2 K is virtually identical to that at 77 K, except that the intrinsic coercive strength is slightly lower.

The magnetic anisotropy energy (ref. 25-30) and the intrinsic coercive strength, of the room-temperature magnetic phase, have been shown to decrease with temperature. These values are reported to reach zero at temperatures of 85 and 80 K, respectively. Neutron diffraction measurements (ref. 25-31) have suggested that small positive values may be found even at very low temperatures. The H_{ci} data for the ASTP ground-based and flight samples support the latter contention to a temperature as low as 4.2 K. Representative curves showing the temperature dependence of the room-temperature magnetic phase, from ground-based and flight samples, are shown in figure 25-27.

At temperatures below room temperature, a second magnetic component having extremely high coercivity appears (ref. 25-24). No magnetic property data, as a function of growth rate, have been published for cryogenic temperatures;

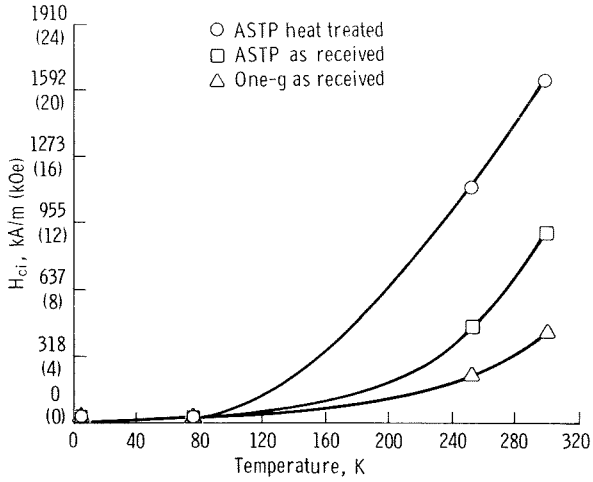

FIGURE 25-27.—Intrinsic coercive strength H_{ci} as a function of temperature for the room-temperature MnBi phase.

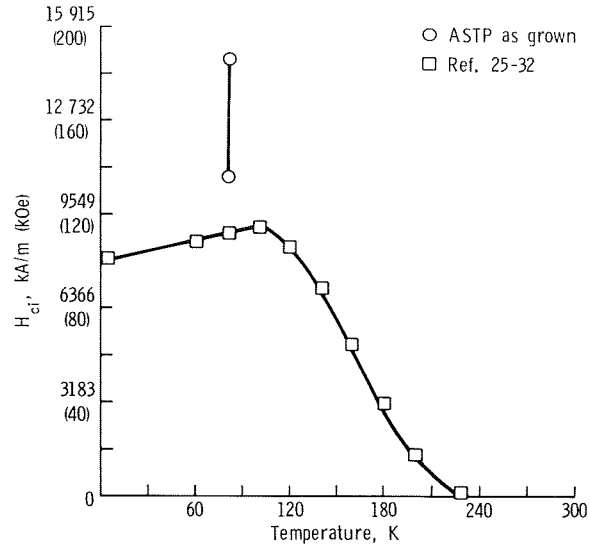

FIGURE 25-28.—Intrinsic coercive strength H_{ci} as a function of temperature for the low-temperature component.

therefore, the ASTP flight-sample low-temperature data have been superimposed on the temperature-dependence results of reference 25-32, as shown in figure 25-28. The literature data shown in figure 25-28 are from samples grown at a rate of 75 cm/hr. It has been reported that the low-temperature component appears only in samples grown at freezing rates in excess of 75 cm/hr (ref. 25-24); however, the ASTP flight data for samples grown at a rate of 3 cm/hr are not consistent with this conclusion.

The average values of intrinsic coercive strength for the ASTP ground-based and flight samples are shown in table 25-II. Work has continued, however, in the analysis of selected sample sections. An unexpected result, but confirmed by other experts on MnBi behavior,[2] is illustrated in figure 25-29. Sections of this type, from the coordinated growth regions of the flight samples, demonstrate the high field coercivity associated with the low-temperature component, but show positive-field "collapse" when field strength is reduced.

Thermal cycling of this sample showed that the positive-field collapse occurred at lower positive fields at 4.2 K than at 77 K. Restated, these results show a wider hysteresis in field strength at 4.2 K than at 77 K.

[2]C. D. Graham, Jr., and M. R. Notis, personal communication.

Some samples were heat treated at 90 percent of the absolute melting point for a period of 24 hours, then furnace cooled. This heat treatment has been reported to substantially improve the

TABLE 25-II.—Intrinsic Coercive Strength as a Function of Test Temperature

[*Average values*]

Sample	*Temperature, K*	*Intrinsic coercive strength, kA/m (kOe)*
ASTP ground-based	295	437.7 (5.5)
ASTP flight		
8C	295	869.0 (10.92)
	253	467.9 (5.88)
	77	10 743.0 (135)
9C	295	1 108.5 (13.93)
	253	870.6 (10.94)
	77	14 721.8 (185)
		11 538.7 (145)
10C	295	814.9 (10.24)
	77	9 350.4 (117.5)
	4.2	8 116.9 (102)
Heat-treated	295	1 655.2 (20.8)
	243	1 040.9 (13.08)
	77	8 753.5 (110)
	4.2	8 116.9 (102)

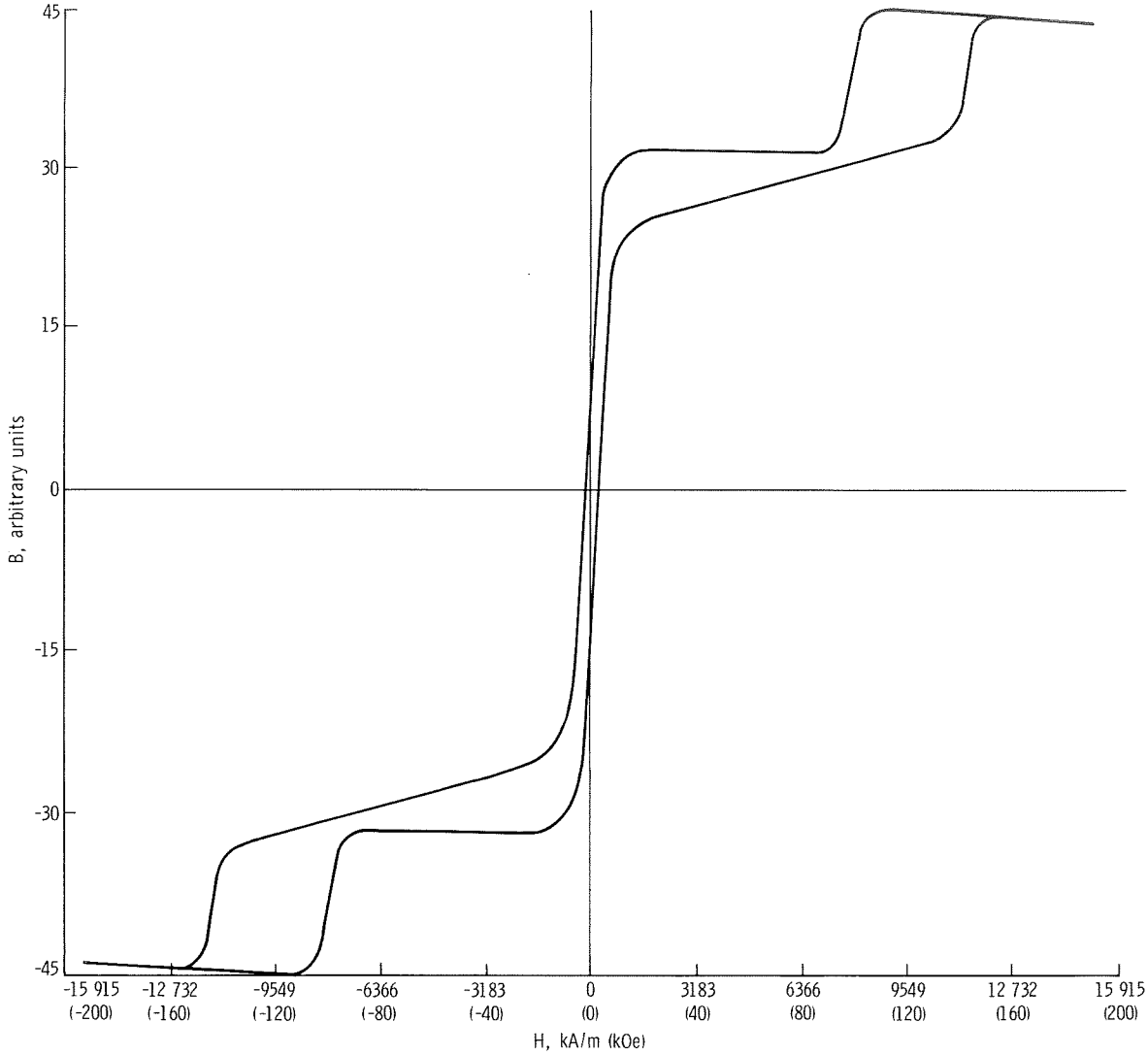

FIGURE 25-29.—As-grown flight sample 9C B-H loop at 77-K test temperature.

room-temperature intrinsic coercive strength. The H_{ci} of this sample increased from 912.8 to 1655.2 kA/m (11.47 to 20.8 kOe), an 80-percent improvement. The heat treatment squared the B-H loop and increased the value of H_{ci} at room temperature, as reported in reference 25-24. The temperature behavior of the room-temperature component of the heat-treated flight sample is shown in figure 25-27. Essentially, the magnitudes are different but the behavior as a function of temperature is consistent.

The heat-treated value of intrinsic coercive strength as a function of rod diameter is shown in figure 25-30. Rod diameter has been selected for the abscissa in this case because the thermal-mechanical state of the composite should be equilibrated. The results indicate that the heat treatment is a determining factor in the final value of H_{ci}. The ASTP data points are entirely consistent with those presented in the literature for similar heat treatments.

A final room-temperature measurement was made on the heat-treated sample. A B-H curve, with the rods transverse to the magnetic field, was measured and is shown in figure 25-31. As may be seen, the sample was not saturated even at the

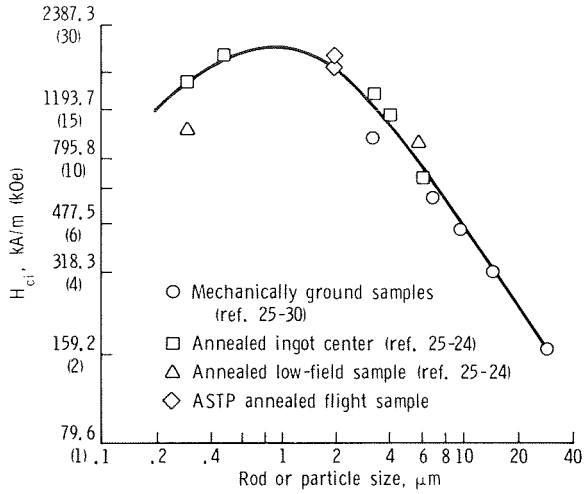

FIGURE 25-30.—Intrinsic coercive strength H_{ci} at room temperature compared to MnBi particle size, for heat-treated MnBi/Bi eutectic composites and mechanically ground MnBi particles.

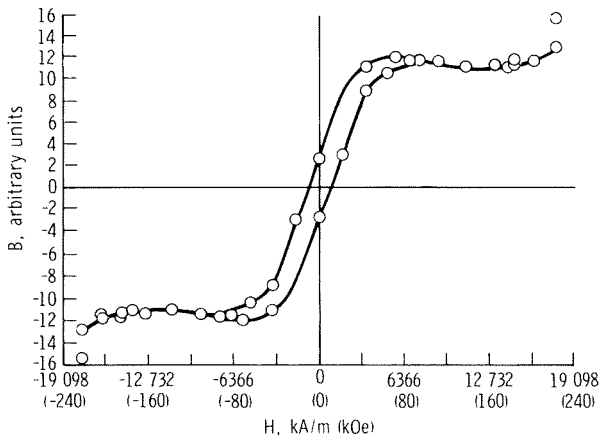

FIGURE 25-31.—Room-temperature B-H loop, with transverse field, for flight sample 11C (heat treated).

highest field strength 22.3 T (223 kG). This result was entirely expected because theoretical estimates (ref. 25-33) of the coercivity in a transverse field predict that saturation will not occur until a field strength of 15 915 to 19 894 kA/m (200 to 250 kOe) has been attained. It would appear that a field of 25 T (250 kG) would be barely adequate for saturation studies.

In addition to intrinsic coercive strength, the magnetization of the ASTP ground-based and flight samples has also been measured. The average magnetization, for magnetic MnBi/Bi eutectic composites, is reported in the literature to be 6 nWb/g (0.6 emu/g) (ref. 25-24). The average value for the ASTP flight samples of 10.5 nWb/g (1.05 emu/g) is a substantial improvement over the previously mentioned value; however, magnetizations an order of magnitude greater were measured within these samples, on their first exposures to a magnetic field. These results could not be reproduced, and subsequent measurements gave the value of 10.5 nWb/g (1.05 emu/g). This variation in magnetization has been noted in a previous study (ref. 25-32) but remains unexplained. The variation indicates that, although the ASTP average value of magnetization has shown improvement over the literature value, an additional improvement may well be possible with proper processing.

In summary, orbital processing of the eutectic MnBi/Bi composite has led to enhanced values of critical magnetic parameters B and H through particle refinement and alinement. The average improvement within these parameters was 60 percent. Although the precise reason for these improvements has not been ascertained, it seems reasonable to presume that the reduction of detrimental gravitationally dependent phenomena, during solidification, has resulted in these improvements in the as-received composites.

The magnetic results from the as-received type 1 samples showed duplex behavior at room temperature. This behavior could be the result of a shift in the onset temperature of the low-temperature magnetic component from 240 to 295 K, or could result from particle size effects. In addition, substantial differences in magnetic behavior were noted, depending on the orientation of the sample in the field. Because the microstructural analysis of the flight samples has shown that the microstructure is complex but nonrandom and that there are substantial differences in the MnBi particle size, it was decided to defer the magnetic analysis of these samples until all the necessary magnetic analyses of the alined, constant-particle-size eutectic samples have been completed.

SUMMARY AND CONCLUSIONS

The intent of this project was to study the contained solidification of magnetic materials in a low-g environment. Although the work is not yet complete, the following conclusions may be drawn.

1. Fluid static configurations in a low-g environment were appreciably different than in one-g, but were found to agree well with theory.

2. Bismuth undergoes a liquid phase transition, with large hysteresis, at temperatures of 988 K on heating and 858 K on cooling.

3. The Mn-Bi phase diagram presented in reference 25-22 is to be preferred.

4. Macroscopic chemical segregation due to gravitationally dependent buoyancy forces is minimal in a low-g environment.

5. The number and size distribution of orbitally processed primary crystals is significantly different in the flight samples.

6. The intrinsic coercive strengths of as-grown low-g MnBi/Bi eutectic samples greatly exceed any values previously reported for this magnetic composite (>60 percent).

7. The solidification product from the orbital processing of the Bi/MnBi faceted rod eutectics differs in particle size and shape, lattice parameter, and magnetic properties from equivalently processed terrestrial samples.

REFERENCES

25-1. Polgreen, G. R.: New Applications of Modern Magnets. Macdonald & Co. (London), 1966.

25-2. Lee, Eric W.: Magnetism. Pelican Books (London), 1963.

25-3. Iden, D. J.; Ehrenfried, C. E.; and Garrett, H. J.: Present and Future Applications of High-Coercive-Force Magnets. Magnetism and Magnetic Materials, AIP Conference Proceedings, no. 5, 1971, p. 1026.

25-4. Strnat, K. J.: The Recent Development of Permanent Magnetic Materials Containing Rare Earth Metals. AFML-TR-69-299, Wright-Patterson AFB, June 1970.

25-5. Becker, Joseph J.; Luborsky, Fred E.; and Martin, D. Luther: Permanent Magnet Materials. IEEE Trans. Magn., vol. MAG-4, no. 2, June 1968, pp. 84-99.

25-6. Hoffer, G.; and Strnat, K.: Magnetocrystalline Anisotropy of YCo_5 and Y_2Co_{17}. IEEE Trans. Magn., vol. MAG-2, no. 3, Sept. 1966, pp. 487-489.

25-7. Strnat, K.; Hoffer, G.; et al.: A Family of New Cobalt-Base Permanent Magnet Materials. J. Appl. Phys., vol. 38, no. 3, Mar. 1, 1967, pp. 1001-1002.

25-8. Buschow, K. H. J.; and Velge, W. A. J. J.: Permanent Magnetic Materials of Rare Earth Cobalt Compounds. Z. Angew. Phys., vol. 26, no. 2, 1969, pp. 157-160.

25-9. Strnat, K. J.: Cobalt-Rare Earth Alloys as Promising New Permanent Magnet Materials. Cobalt, vol. 36, Sept. 1967, pp. 133-143.

25-10. Nesbitt, E. A.: New Permanent Magnet Materials Containing Rare-Earth Metals. J. Appl. Phys., vol. 40, no. 3, Mar. 1, 1969, pp. 1259-1265.

25-11. Faltermayer, Edmund: The Energy "Joyride" Is Over. Fortune, vol. 86, no. 3, Sept. 1972, pp. 99-101.

25-12. Prototype Test Report for MA-010 Experiment Cartridges. Tech. Rep. WANL-TME-2867, Westinghouse Electric Corp., Astronuclear Lab., May 1975.

25-13. Thermal Analysis of the Apollo Soyuz Test Project MA-070 Experiment in the Flight Environment. Tech. Letter ASD-EP44-22740 (SO-E017-Par III) H72, Teledyne Brown Engineering, Jan. 21, 1976.

25-14. Witt, A. F.; Gatos, H. C.; et al.: Steady State Growth and Segregation Under Zero Gravity: InSb. Proceedings of the Third Space Processing Symposium—Skylab Results. NASA TM X-70252, 1974, pp. 275-288.

25-15. Hasemeyer, Earl A.; Lovoy, Charles V.; and Lacy, L. L.: Skylab Experiment M566 Copper-Aluminum Eutectic. Proceedings of the Third Space Processing Symposium—Skylab Results. NASA TM X-70252, 1974, pp. 457-461.

25-16. Clodfelter, Robert G.; and Lewis, Roger C.: Fluid Studies in a Zero Gravity Environment. Tech. Note 61-84, Wright-Patterson AFB, June 1961.

25-17. Clodfelter, Robert G.: Fluid Mechanics and Tankage Design for Low Gravity Environments. ASD-TDR-63-506, Wright-Patterson AFB, Sept. 1963.

25-18. Clodfelter, Robert Glen: Low Gravity Pool Boiling Heat Transfer. APL-TDR-64-19, Wright-Patterson AFB, Mar. 1964.

25-19. Vezzoli, Gary C.: Electrical Resistance of Liquid Sulfur to 420° C and of Liquid Selenium to 700° C. American Ceram. Soc. J., vol. 55, no. 2, Feb. 1972, pp. 65-67.

25-20. Hansen, Max: Constitution of Binary Alloys. McGraw-Hill Book Co., 1958, pp. 318-321.

25-21. Willis, B. T. M.; and Rooksby, H. P.: Magnetic Transitions and Structural Changes in Hexagonal Manganese Compounds. Proc. Phys. Soc. (London), vol. 67B, Apr. 1954, pp. 290-296.

25-22. Chen, Tu; and Stutius, W. E.: The Phase Transformation and Physical Properties of the MnBi and $Mn_{1.08}Bi$ Compounds. IEEE Trans. Magn., vol. MAG-10, no. 3, Sept. 1974, pp. 581-586.

25-23. Hunt, J. D.; and Jackson, K. A.: Binary Eutectic Solidification. Trans. Met. Soc. AIME, vol. 236, no. 6, June 1966, pp. 843-852.

25-24. Boulbes, J. C.; Kraft, R. W.; Notis, M. R.; and Graham, C. D., Jr.: Structural and Magnetic Properties of the Bi-MnBi Controlled Eutectic. Proceedings of the Conference on *In Situ* Composites, Vol. III, National Materials Advisory Board Spec. Publ. 308, Jan. 1973, pp. 61-78.

25-25. Cline, H. E.; and Livingston, J. D.: High-Speed Directional Solidification of Sn-Pb Eutectic Alloys. Trans. Met. Soc. AIME, vol. 245, no. 9, Sept. 1969, pp. 1987-1992.

25-26. Verhoeven, J. D.; Warner, J. C.; and Gibson, E. D.: Effect of Thermotransport Upon Off-Eutectic Composite Growth in Sn-Pb Alloys. Met. Trans., vol. 3, no. 6, June 1972, pp. 1437-1441.

25-27. Albright, D. L.; Conard, G. P., II; and Kraft, R. W.: Magnetic Behavior of a Eutectic Alloy Featuring an Aligned Array of Iron Rods. J. Appl. Phys., vol. 38, no. 7, June 1967, pp. 2919-2923.

25-28. Stoner, E. C.; and Wohlfarth, E. P.: A Mechanism of Magnetic Hysteresis in Heterogeneous Alloys. Phil. Trans. Roy. Soc. London, vol. A240, May 1948, pp. 599-642.

25-29. Foner, Simon: Versatile and Sensitive Vibrating-Sample Magnetometer. Rev. Sci. Instrum., vol. 30, no. 7, July 1959, pp. 548-557.

25-30. Guillaud, C.: Ferromagnetism of Binary Alloys. Ph. D. Thesis, Univ. of Strasbourg, 1943.

25-31. Roberts, B. W.: Neutron Diffraction Study of the Structures and Magnetic Properties of Manganese Bismuthide. Phys. Rev., vol. 104, no. 3, Nov. 1, 1956, pp. 607-616.

25-32. Boulbes, J. C.: Structural and Magnetic Properties of the Bi-Mn-Bi and Controlled Eutectics. M. S. Thesis, Lehigh Univ., 1971.

25-33. Noothoven van Goor, J. M.; and Zijlstra, H.: Structural and Magnetic Properties of a Bi-MnBi Composite, J. Appl. Phys., vol. 39, no. 12, Nov. 1968, pp. 5471-5474.